Fusion Engineering and Design 205 (2024) 114527

Contents lists available at ScienceDirect

Fusion Engineering and Design

journal homepage: www.elsevier.com/locate/fusengdes

On the accuracy of a fast time resolution inversion method for the detection of different radiation patterns in fusion reactors

Ivan Wyss [a,*], Andrea Murari [b,c], Emmanuele Peluso [a], Michela Gelfusa [a], Pasquale Gaudio [a], Riccardo Rossi [a]

[a] Department of Industrial Engineering, University of Rome "Tor Vergata", Via del Politecnico 1, 00133 Rome, Italy
[b] Consorzio RFX (CNR, ENEA, INFN, Università di Padova, Acciaierie Venete SpA), Corso Stati Uniti 4, 35127 Padova, Italy
[c] Istituto per la Scienza e la Tecnologia dei Plasmi, CNR, Padova, Italy

ARTICLE INFO

Keywords:
Tomography
Plasma operation
Disruption
Anomaly radiation
Bolometry
Fast inversion

Accurate measurements of the emitted radiation are crucial for controlling a fusion reactor. In addition to affecting the global power balances, high levels of local radiation emission can indicate that the plasma is losing stability and can disrupt. Several radiation events can occur in a tokamak differing in localization, shape, and dimension. Each of these can be originated by various causes and degrade the plasma confinement in different ways. On current tokamaks, radiation is measured by bolometers, but these provide only line integrated values. For this reason, quite sophisticated tomography inversion algorithms are required to obtain local information, but this approach is slow and cannot be used in real time yet. A fast inversion method, which provides local information with high temporal resolution, has been developed. This allows to reconstruct the emissivity in all the relevant regions of the plasma and so to recognize different anomalous radiation events. In this work, an analysis of the fast inversion method and of its performances is presented using synthetic data. The reliability of the method is tested by simulating different patterns of radiation. Then the accuracy is evaluated by analysing the impact of different features, such as shape and position, on the reconstruction.

1. Introduction

Nuclear fusion holds great promise as a solution for clean energy production. One approach to achieving nuclear fusion reactions involves the confinement of a high-temperature plasma using magnetic fields. The most advanced device of this type is the tokamak. While recent technological advancements have enabled to make significant progresses in this field, there remain challenges that delay the ability to sustain continuous fusion reactions. Specifically, various types of instabilities can occur within a tokamak plasma, leading to a degradation of confinement and potentially causing disruptions [1,2]. Identifying these instabilities is a crucial task in controlling the fusion process, with the aim of rendering the plasma stable and preventing disruptions [3–6]. Some of these instabilities are associated with unusual patterns of radiation emission. Therefore, monitoring radiation emissions and determining their source play a crucial role in preventing disruptions [7–12]. At present, radiation measurements are conducted using various techniques such as bolometers, soft X-rays, and others, each focusing on different segments of the electromagnetic spectrum [13,14]. However, these methods yield only integrated values along a line of sight, necessitating the use of tomographic inversion algorithms to obtain localized information. While tomographic techniques can offer high spatial resolution and accurate estimates, they are typically too slow for real-time applications [15]. Moreover, tomographic inversion is a mathematically ill-posed problem that requires regularization functions, which must be calibrated for each specific experiment [16]. In this work, we analyse the performances of the new high-time low-spatial resolution tomographic inversion [17], which allows estimating the average local emissivity in specific regions of the poloidal section without imposing stringent constraints. Section 2 investigates the principles and techniques behind this rapid tomographic inversion method. In Section 3, this methodology is tested using synthetic data to substantiate its accuracy and effectiveness. Finally, in Section 4, we discuss the key findings and conclusions drawn from our research.

2. Fast tomography inversion

Tomographic inversion utilizes line-integrated measurements to reconstruct local information [18,19]. In this study, our primary focus is on its application to bolometers for the estimation of the plasma total

* Corresponding author.
E-mail address: ivan.wyss@uniroma2.it (I. Wyss).

https://doi.org/10.1016/j.fusengdes.2024.114527
Received 20 October 2023; Received in revised form 24 May 2024; Accepted 24 May 2024
Available online 8 June 2024

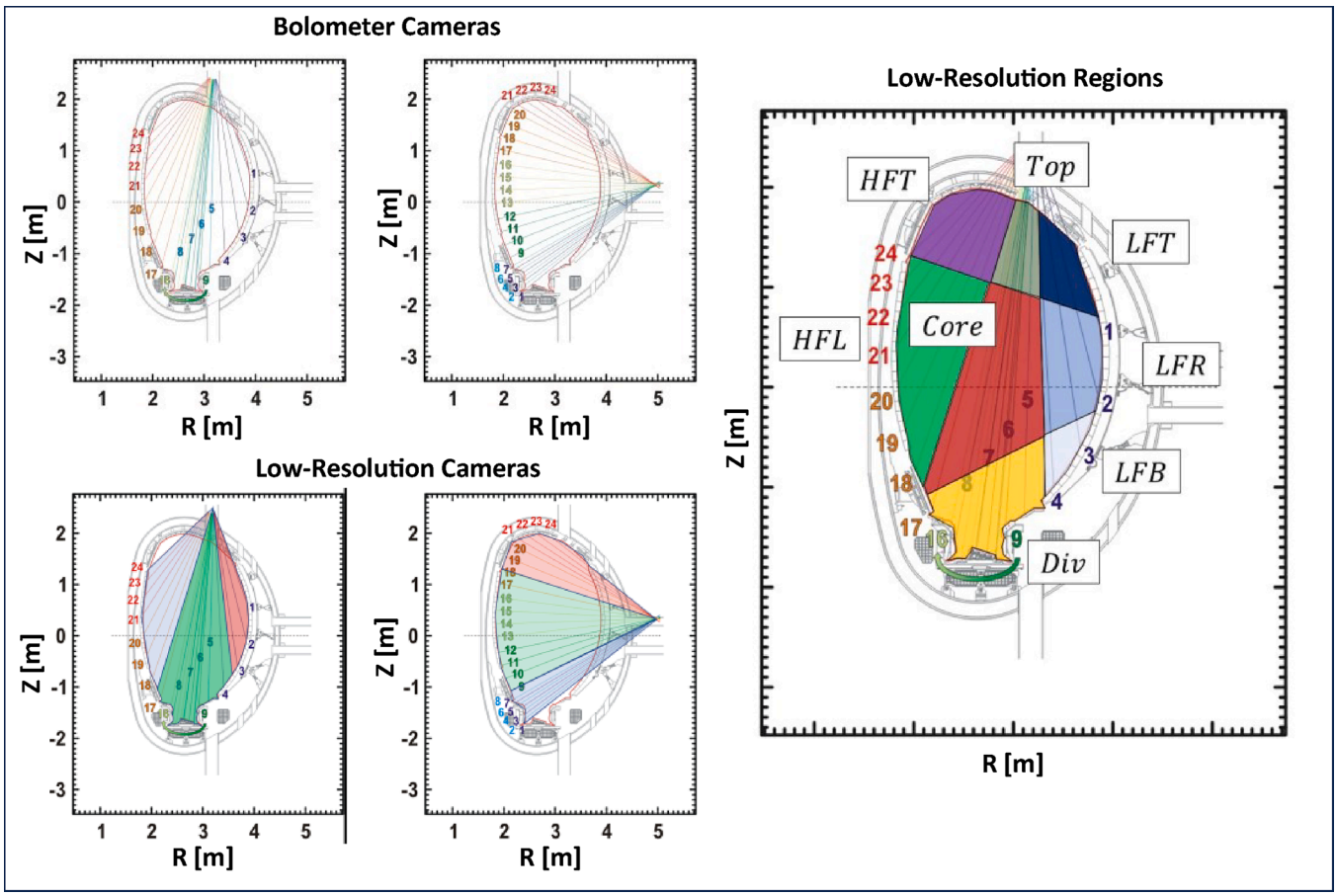

Fig. 1. (a) Lines of sight of bolometer cameras in JET. (b)) Lines of sight collected together forming the six macro-views. (c) The eight regions of the fast tomography. The acronyms in plot (c) stand for: HFL: High Field Low, HFT: High Field Top; LFT: Low Field Top; LFR: Low Field Right; LFB: Low Field Bottom.

radiation emission, but this methodology can also be applied to other diagnostics [20–22]. Even if this work is based on synthetic cases, the Joint European Torus (JET) geometry and bolometer lines of sight are used as reference [23,24]. The transfer to other geometries, tokamaks, and diagnostics does not pose any conceptual problem but might require some specific adjustments.

JET bolometric system consists of two cameras: one horizontal and one vertical. Each camera provides 24 lines of sight, slicing through the poloidal cross-section, as shown in Fig. 1(a). Each line of sight, identified with the subscript "m", measures the line-integrated emissivity g_m, *so that:*

$$g_m = \int_{l_m} \epsilon \, dl \tag{1}$$

where l_m is the m-th line of sight length and ε the plasma emissivity. The local emissivity is reconstructed on a matrix of n pixels. Then, the reconstructed line-of-sight measurements given the emissivity matrix should be equal to the actual measurements:

$$g_m = \sum_n H_{mn}\epsilon_n \tag{2}$$

where H_{mn} represents the contribution of pixel *n* to the overall measurement *m*. Therefore, starting from the m measurements, in principle tomography could provide the emissivity ε_n for each pixel by inverting Eq. (2). This inversion poses a challenge though, as it is an ill-posed problem (n, the number of unknowns, is usually much larger than m, the number of equations), requiring regularization to obtain a solution consistent with the expected physics [25]. Various approaches are used to address this issue, but they often demand significant computational resources or extensive calibration using a large set of experimental measurements. The aim of this method is to offer a rapid emissivity reconstruction without making assumptions about regularization or necessitating training [26,27].

The key concept is to reduce the grid size, significantly reducing the number of unknowns and, consequently, the computational demand for inversion. While reducing the grid can introduce inaccuracies in the reconstruction, careful definition of the macrogrid allows us maintaining sufficient resolution and accuracy in detecting anomalous radiation from different regions of the plasma. This is achieved by assuming the existence of three macroscopic views for each camera, formed by grouping the corresponding lines of sight as shown in the Fig. 1(b). The intersection of these lines defines eight distinct regions Fig. 1(c). With this configuration, the tomographic inversion task requires solving the following set of equations:

$$\begin{aligned}
g_{H_1} &= \varepsilon_{\mathrm{Div}} H_{\mathrm{Div},H_1} + \varepsilon_{\mathrm{LFB}} H_{\mathrm{LFB},H_1} \\
g_{H_2} &= \varepsilon_{\mathrm{HFL}} H_{\mathrm{HFL},H_2} + \varepsilon_{\mathrm{Core}} H_{\mathrm{Core},H_2} + \varepsilon_{\mathrm{LFR}} H_{\mathrm{LFR},H_2} \\
g_{H_3} &= \varepsilon_{\mathrm{HFT}} H_{\mathrm{HFT},H_3} + \varepsilon_{\mathrm{Top}} H_{\mathrm{Top},H_3} + \varepsilon_{\mathrm{LFT}} H_{\mathrm{LFT},H_3} \\
g_{V_1} &= \varepsilon_{\mathrm{LFB}} H_{\mathrm{LFB},V_1} + \varepsilon_{\mathrm{LFR}} H_{\mathrm{LFR},V_1} + \varepsilon_{\mathrm{LFT}} H_{\mathrm{LFT},V_1} \\
g_{V_2} &= \varepsilon_{\mathrm{Div}} H_{\mathrm{Div},V_2} + \varepsilon_{\mathrm{Core}} H_{\mathrm{Core},V_2} + \varepsilon_{\mathrm{Top}} H_{\mathrm{Top},V_2} \\
g_{V_3} &= \varepsilon_{\mathrm{HFT}} H_{\mathrm{HFT},V_3} + \varepsilon_{\mathrm{HFL}} H_{\mathrm{HFL},V_3}
\end{aligned} \tag{3}$$

Here, *g* represents the line-integrated measurement of the macroscopic line evaluated as the sum of the collected lines, *ε* indicates the emissivity, and *H* stands for the contribution of the corresponding region. This system of equations consists of six equations with eight unknowns. When we introduce non-negativity soft constraints (4) for each emissivity R, these equations become readily invertible.

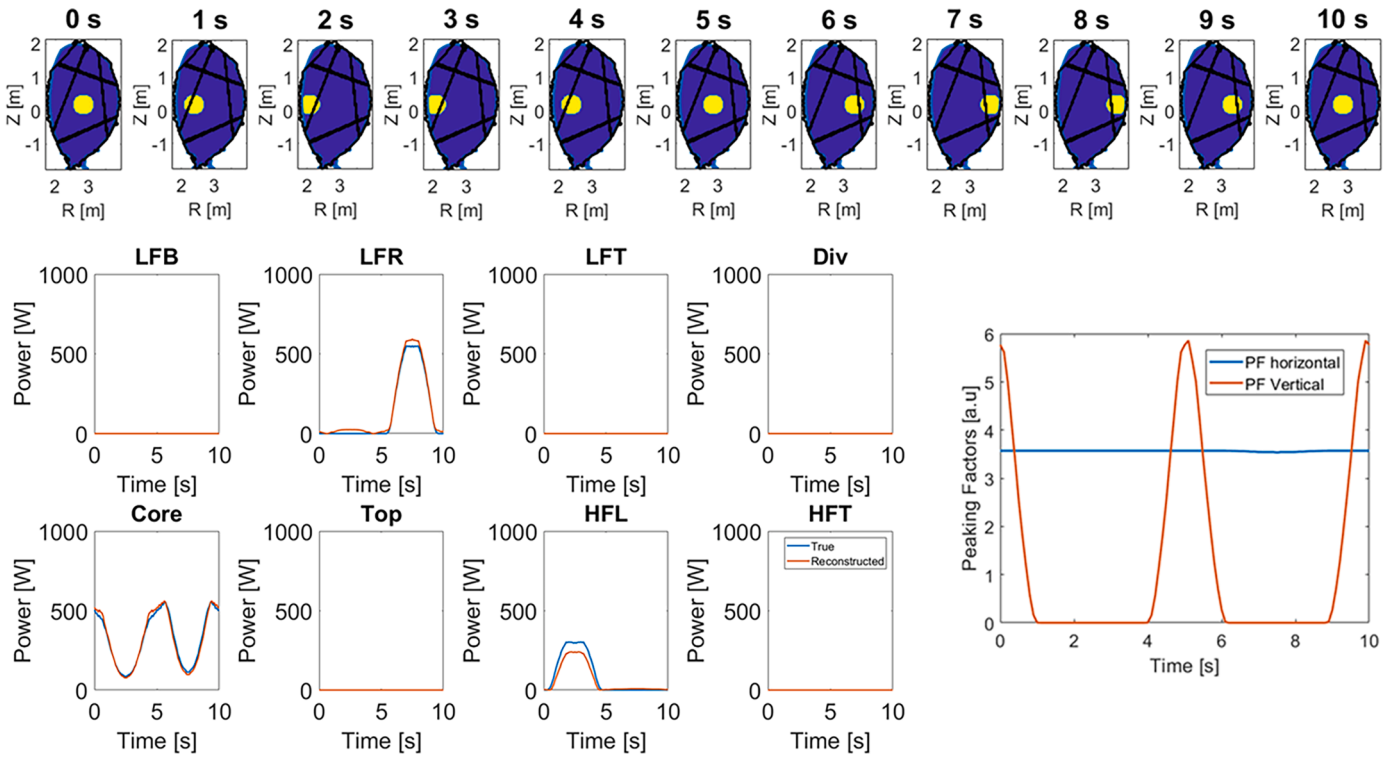

Fig. 2. (Upper) The numerical built emissivity through the time. (Bottom Left). The power in the eight regions, both numerical calculated and reconstructed. (Bottom right) Calculated peaking factors.

$$\varepsilon_{region} \geq 0 \tag{4}$$

The system of Eqs. (3) has been solved by using a simple non-negative least square minimisation method [28]. By following this strategy, it is possible to achieve rapid reconstruction of these 8 important regions in less than 50 μs per time slice, without relying on any *a priori* knowledge, while ensuring that radiation remains positively

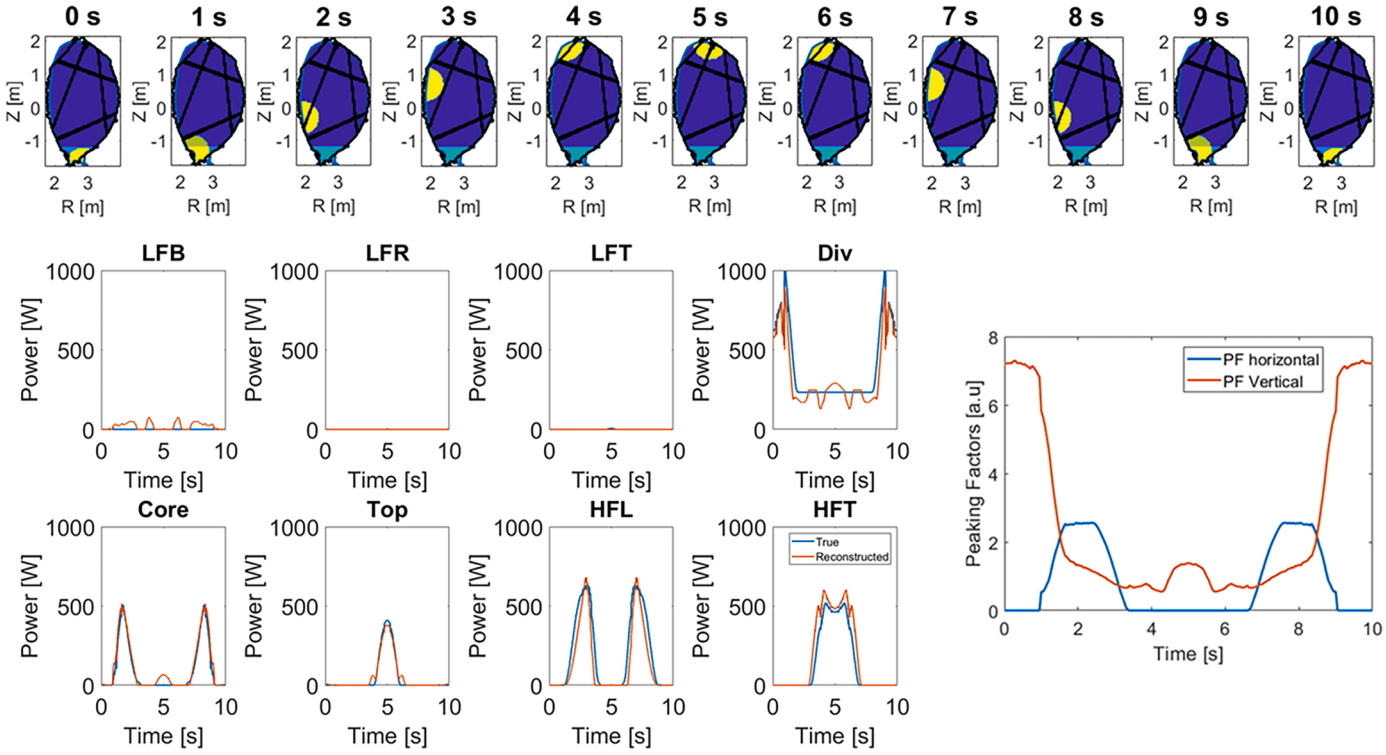

Fig. 3. (Upper) The evolution of the numerical emissivity phantom with the time. (Bottom Left). The power in the eight regions of Fig. 1, both numerically calculated using the phantom (blue) and reconstructed (red). (Bottom right) Evolution of the peaking factors vs time showing that they cannot always identify properly the location of the emission. (For interpretation of the references to color in this figure legend, the reader is referred to the web version of this article.)

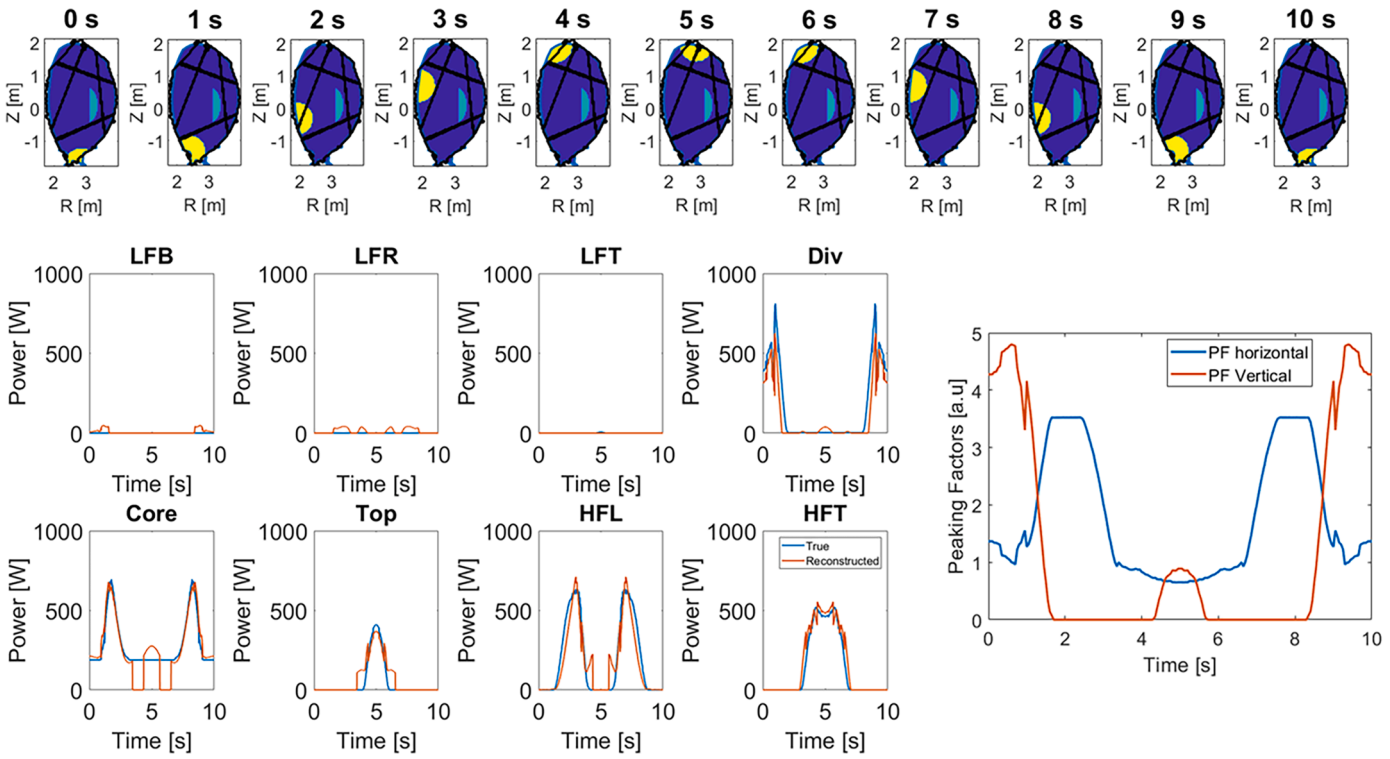

Fig. 4. (Upper) The evolution of the numerical emissivity phantom with the time. (Bottom Left). The power in the eight regions of Fig. 1, both numerically calculated using the phantom (blue) and reconstructed (red). (Bottom right) Evolution of the peaking factors vs time showing that they cannot always identify properly the location of the emission. (For interpretation of the references to color in this figure legend, the reader is referred to the web version of this article.)

valued.

3. Numerical tests

In this section, we present an analysis using numerical phantoms. Three synthetic cases are shown, which accurately reflect important anomalously radiating phenomena observed in experiments. The objective of this analysis is to prove the method capability to identify the emitting region, to trace its motion within the plasma, and additionally to compare the results with the traditional indicators reported in the literature and called peaking factors [14]. The 48 lines of sight for each phantom have been calculated and then combined to determine the emission from the macro-regions of the high time resolution tomography. It has been decided to simulate three 10 s plasma discharges with a time resolution of 10 ms. For each case, the synthetic radiation patterns scan the entire parts of the poloidal cross section covered by the corresponding radiative features in the actual JET experiments.

3.1. Moving central blob

In this example, a radiative blob traversing the poloidal section, progressing from the low-field side to the high-field side, is simulated as illustrated in Fig. 2 (Upper). The circular blob has a radius of 0.3 m and homogeneous emissivity of 100 W/m^3.The 10 phantoms presented represent only a subset of the complete simulated discharge, which comprises a thousand instances. They are shown to provide an overview of the movement evolution. From the fast tomography inversion, the power radiated for each of the 8 regions is obtained as shown in Fig. 2 (Bottom left). By examining these values, the trajectory of the blob across the poloidal section becomes easily discernible. In fact, at time 0, a high radiation value can be observed only in the core, then it starts to decrease while increasing in the HFL, indicating the transfer of radiation from one region to the other. After 2.5 s, the radiation in the HFL decreases, increasing again in the core. The same mechanism can be observed from 5 s from the Core towards the LFR. In this way, by observing the decrease in radiation in one region and the corresponding increase in another, it is possible to determine the movement of the blob from the reconstructed powers. However, the peaking factors hold less significance in this context as they do not manage to identify the anomalous region with the same accuracy, see Fig. 2 (Bottom right). This is a very important aspect because depending on the emitting regions completely different remedial actions can be appropriate as discussed in [27]. Indeed, the fact that the horizontal peaking factor tends to be unnecessarily high can generate false alarms in many situations, as discussed in detail in [17]. The vertical one in its turn can detect only radiation anomalies in the center, whereas acting earlier when the radiation increases at the edge can make the difference between success and failure of control strategies.

3.2. MARFE-like

In this example a radiative blob moving along the wall in the high field region has been generated, simulating a MARFE-like anomaly [29], combined with an emission from the divertor, see Fig. 3 (Upper). This example, with two regions of high emission simultaneously present, is particularly challenging for any reconstruction method, given the layout of JET diagnostic. The blob simulating the MARFE is circular with homogeneous emissivity of 100 W/m^3. It has been made to move along the edge on the high field side, from $-\pi/2$ to $+\pi/2$ (angle calculated from the centre of the cross-section). The shape is determined by the intersection with the vessel, which cuts it. The radiation pattern in the divertor is constant and homogeneous, emitting 50 W/m^3 for $Z<-1.2$ m.

From the power reconstructed the fast tomography can easily track the MARFE evolution (Fig. 3 Bottom left). Indeed, it is possible to observe the reconstructed power varying through time. Initially, the peak power is localized in the divertor region, subsequently transitioning through the midplane, progressing upward in the high-field area, and ultimately reaching the top. By observing the increase in radiation

Table 1
The error in the various regions, calculated as the average relative difference between the power emitted by the radiation patterns and the reconstructed values in the respective macro-regions over the entire time interval, expressed in percentage.

Case	P tot	LF down	LF right	LF up	Divertor	Core	Top	HF Left	HF Top
Moving Blob	−1.7 %	–	5.1 %	–	–	0.8 %	–	−24.6 %	–
MARFE	−2.8 %	–	–	–	−10.1 %	5.2 %	−6.9 %	−15.3 %	19.8 %
MARFE and Asymmetry	−3.7 %	–	–	–	−20.0 %	4.2 %	−10.0 %	−13.7 %	6.1 %

in one region and the decrease in another, it is possible to determine the movement of the MARFE.

3.3. MARFE-like and crescent shape core emission

In this example, the evolution of a MARFE is depicted with an asymmetric emission in the core region, as illustrated in Fig. 4 (Upper). The feature simulating the MARFE presents homogeneous emissivity of 100 W/m^3. It is a circular blob moving along the edge, covering angle from $-\pi/2$ to $+\pi/2$ calculated from the centre of the cross-section. The shape is determined by the intersection with the vessel, which cuts it. The crescent shape radiation pattern is homogeneous and equal to 50 W/m^3. Its shape is a portion of a circle of radius 0.75 m, with centre in $R = 2.6$ m and $Z=-0.1$ m, cut with a plane at 3.1 m.

Similarly to previous example, in this case, it is possible to trace the movement of the MARFE through the reconstructed power in different regions, as shown in Fig. 4(Bottom Left). Once again, the anomalous radiation can be observed from the peaking factors Fig. 4 (Bottom Right) but determining the specific region of excessive emission would be very challenging.

In Table 1 the reconstruction error of the fast tomography is reported for each region and for the total emitted power.

The error E is evaluated as in [30], as reported in Eq. (5)

$$E = \frac{P_{reg,C} - P_{regP}}{P_{regP}} \times 100\ \% \tag{5}$$

where $P_{reg,C}$ is the one obtained for each region by the fast tomography and $P_{reg,P}$ is the one referred to the phantom. E is evaluated at each instant and then averaged over the entire duration. The error calculated in the three cases for the total power remains below 4 %, while the error in the individual regions on average is below 20 %. Although this is an acceptable error threshold, it should be considered that this is influenced by the errors assessed during moments when the power in the region is low, which can result in a large error.

4. Conclusions

In this paper, the performances of the new technique for obtaining a fast tomography reconstruction have been analysed. The potential of this approach has been substantiated by simulating different radiation patterns. The reported results show that:

- The fast tomography is quite accurate in reconstructing the radiation emission in the most important regions for stability on JET [27].
- This advancement enables precise tracking of anomalous radiation movements within the plasma, improving disruption avoidance strategies [27].
- The fast tomography significantly improves the bolometric diagnostic capability of pinpointing emission sources in real time, compared to the most used global indicators such as the peaking factors as shown in detail in [17]

It has also been checked that adding to all the phantoms a reasonable level of background emission, comparable to the diffuse emission encountered in practice, does not change in any significant way the reported results. On the other hand, in terms of maximum resolution, of course only radiation patterns that have a significant size and intensity relative to the macropixels can be detected. Small scale structures and movements cannot be resolved, unless their emission is significantly higher than the background radiation of the macropixels, in which they are located.

Future developments will be focussed on defining and testing an avoidance strategy in other working machines using this new procedure to estimate the total radiation emission. Moreover, the methodology will be proposed for other tokamaks, such as ASDEX-Upgrade and TCV, so that a standard and multi-machine approach may be used for tokamak control. Of course given the fact that bolometric diagnostics have different layouts in different devices, the transfer of the approach will require specific investigations and adaptations.

CRediT authorship contribution statement

Ivan Wyss: Writing – review & editing, Writing – original draft, Validation, Software, Methodology, Data curation, Conceptualization. **Andrea Murari:** Writing – review & editing, Visualization, Supervision, Conceptualization. **Emmanuele Peluso:** Resources, Conceptualization. **Michela Gelfusa:** Supervision, Project administration. **Pasquale Gaudio:** Supervision, Project administration. **Riccardo Rossi:** Validation, Software, Methodology, Conceptualization.

Declaration of competing interest

The authors declare no conflict of interest.

Data availability

Data will be made available on request.

Acknowledgements

This work has been carried out within the framework of the EUROfusion Consortium, funded by the European Union via the Euratom Research and Training Programme (Grant Agreement No 101052200 — EUROfusion). Views and opinions expressed are however those of the author(s) only and do not necessarily reflect those of the European Union or the European Commission. Neither the European Union nor the European Commission can be held responsible for them.

References

[1] W. Suttrop et al., “Tearing Mode Formation and radiative edge cooling prior to density limit disruptions in Asdex Upgrade,” 1997.
[2] V. Igochine, “Active Control of Magnetohydrodynamic Instabilities in Hot Plasmas.” [Online]. Available: http://www.springer.com/series/411.
[3] R. Wenninger et al., “Power Handling and Plasma Protection Aspects that affect the Design of the DEMO Divertor and First Wall”.
[4] T.C. Hender, et al., Chapter 3: MHD stability, operational limits and disruptions, Nucl. Fusion 47 (6) (2007) S128, https://doi.org/10.1088/0029-5515/47/6/S03.
[5] G. Pucella, et al., Onset of tearing modes in plasma termination on JET: the role of temperature hollowing and edge cooling, Nucl. Fusion 61 (4) (2021), https://doi.org/10.1088/1741-4326/ABE3C7.
[6] C. Sozzi et al., “Termination of discharges in high Performance scenarios in JET”.
[7] J. Vega, et al., Disruption prediction with artificial intelligence techniques in tokamak plasmas, Nat. Phys. 18 (7) (2022) 741–750, https://doi.org/10.1038/s41567-022-01602-2.

[8] A. Murari, E. Peluso, M. Lungaroni, R. Rossi, M. Gelfusa, Investigating the physics of tokamak global stability with interpretable machine learning tools, Appl. Sci. 10 (19) (2020) 6683, https://doi.org/10.3390/APP10196683.
[9] A. Murari, et al., On the transfer of adaptive predictors between different devices for both mitigation and prevention of disruptions, Nucl. Fusion 60 (5) (2020) 056003, https://doi.org/10.1088/1741-4326/AB77A6.
[10] A. Murari, et al., Adaptive predictors based on probabilistic SVM for real time disruption mitigation on JET, Nucl. Fusion 58 (5) (2018) 056002, https://doi.org/10.1088/1741-4326/AAAF9C.
[11] A. Murari, R. Rossi, T. Craciunescu, J. Vega, M. Gelfusa, A control oriented strategy of disruption prediction to avoid the configuration collapse of tokamak reactors, Nat. Commun. 15 (1) (2024) 1–19, https://doi.org/10.1038/s41467-024-46242-7.
[12] E.J. Strait, et al., Progress in disruption prevention for ITER, Nucl. Fusion 59 (11) (2019) 112012, https://doi.org/10.1088/1741-4326/AB15DE.
[13] R. Rossi, M. Gelfusa, J. Flanagan, A. Murari, Development of robust indicators for the identification of electron temperature profile anomalies and application to JET, Plasma Phys. Control Fusion. 64 (4) (2022), https://doi.org/10.1088/1361-6587/ac4d3b.
[14] A. Pau, et al., A first analysis of JET plasma profile-based indicators for disruption prediction and avoidance, IEEE Trans. Plasma Sci. 46 (7) (2018) 2691–2698, https://doi.org/10.1109/TPS.2018.2841394.
[15] M. Odstrcil, J. Mlynar, T. Odstrcil, B. Alper, A. Murari, Modern numerical methods for plasma tomography optimisation, Nucl. Instrum. Methods Phys. Res. a 686 (2012) 156–161, https://doi.org/10.1016/j.nima.2012.05.063.
[16] J. Mlynar, et al., Current research into applications of tomography for fusion diagnostics, J. Fusion Energy 38 (3–4) (2019) 458–466, https://doi.org/10.1007/s10894-018-0178-x.
[17] I. Wyss et al., "Comparison of a fast low spatial resolution inversion method and peaking factors for the detection of anomalous radiation patterns and disruption prediction," 2023, 10.1016/j.fusengdes.2023.113625.
[18] L.C. Ingesson, B.J. Peterson, and J.-C. Vallet, "Chapter 7 Tomography Diagnostics: Bolometry And Soft-X-Ray Detection.".
[19] T. Odstrčil, T. Pütterich, M. Odstrčil, A. Gude, V. Igochine, U. Stroth, Optimized tomography methods for plasma emissivity reconstruction at the ASDEX upgrade tokamak, Rev. Sci. Instrum. 87 (12) (2016), https://doi.org/10.1063/1.4971367.
[20] T. Craciunescu, E. Peluso, A. Murari, M. Gelfusa, Maximum likelihood bolometric tomography for the determination of the uncertainties in the radiation emission on JET TOKAMAK, Rev. Sci. Instrum. 89 (5) (2018), https://doi.org/10.1063/1.5027880.
[21] T. Craciunescu, et al., The maximum likelihood reconstruction method for JET neutron tomography, Nucl. Instrum. Methods Phys. Res. a 595 (3) (2008) 623–630, https://doi.org/10.1016/j.nima.2008.07.145.
[22] M. Ruiz, et al., Acceleration of an algorithm based on the maximum likelihood bolometric tomography for the determination of uncertainties in the radiation emission on JET using heterogeneous platforms, Appl. Sci. 12 (13) (2022), https://doi.org/10.3390/app12136798.
[23] A. Huber et al., "Improved radiation measurements on JET-First results from an upgraded bolometer system", 10.1016/j.jnucmat.2007.01.124.
[24] A. Huber, et al., Upgraded bolometer system on JET for improved radiation measurements, Fusion Eng. Des. 82 (5–14) (2007) 1327–1334, https://doi.org/10.1016/j.fusengdes.2007.03.027.
[25] M. Anton et al., "X-ray tomography on the TCV tokamak," 1996.
[26] F.A. Matos, D.R. Ferreira, P.J. Carvalho, Deep learning for plasma tomography using the bolometer system at JET, Fusion Eng. Des. 114 (2017) 18–25, https://doi.org/10.1016/J.FUSENGDES.2016.11.006.
[27] R. Rossi, et al., A systematic investigation of radiation collapse for disruption avoidance and prevention on JET tokamak, in: Matter Radiat. Extrem., 8, 2023, https://doi.org/10.1063/5.0143193.
[28] C.L. Lawson, R.J. Hanson, Solving least squares problems, Solv. Least Squares Probl. (1995), https://doi.org/10.1137/1.9781611971217.
[29] B. Lipschultz et al., "MARFE: an edge plasma phenomenon".
[30] P. David, M. Bernert, T. Pütterich, C. Fuchs, S. Glöggler, T. Eich, Optimization of the computation of total and local radiated power at ASDEX Upgrade, Nucl. Fusion 61 (6) (2021), https://doi.org/10.1088/1741-4326/abf2e1.